

Fig. 5. Apparatus diagram. A cross-section of the electrostatic lens assembly including field lines and ion trajectories is shown.

2. Experimental Section

2.1. Apparatus

Figure 5 shows the key to velocity mapping — an electrostatic immersion lens assembly⁴ — which is simply a set of three flat circular electrodes shown in cross-section. Since the goal of the apparatus is to measure only the recoil velocity of photofragment ions, it is important to minimize the effects of the parent molecule velocity. Entraining the molecule in the supersonic expansion of a pulsed molecular beam, which cools the molecular velocity component transverse to the detection axis down to a few degrees Kelvin or less, does this. The molecular beam passes through a small hole in the first (repeller) electrode where it is intersected at right angles by the photodissociation/REMPI laser(s). An electric field between the repeller and the second (extractor) electrode accelerates the formed ions past the third (ground) electrode, and through a “field-free” time-of-flight (TOF) region and onwards to the 2-D ion detector. The extractor and ground electrodes are thin metal plates with a 15 mm open circle at the middle,

and the repeller-extractor and extractor-ground electrode spacing is 20 mm. Variations in these opening/distance ratios yield similar results. Field lines are shown in Fig. 5 for repeller: extractor voltages of 1000 V : 750 V. Due to the open electrode structure, the field lines penetrate out of the extractor-ground region, forming the electrostatic lens. With the ionization geometry so chosen, the electrostatic lens, when set properly, has the amazing property of projecting out the velocity of each formed, independent of where the ion was formed in the laser focus. This is critical because the REMPI laser creates a line of ions across the diameter of the molecular beam. Each point along this line acts as an origin for a Newton sphere, which with a normal linear projection would lead to significant “blurring” of the image along the direction of the laser beam. In conventional ion imaging, a “normal” linear projection is produced by covering the electrode openings with a fine metal gauze. This gives the advantage of a direct 1:1 mapping relation ($v = R/\text{TOF}$), where R is the transverse distance from the detector axis at the position-sensitive detector (PSD) and TOF is the time-of-flight needed to reach the detector with the laser pulse as time zero. Linear projection suffers from the above mentioned “blurring”, and in addition, the gauze causes deflections and blocking of the ions as they pass through it. With the simple open structure of the three-electrode electrostatic lens, 100% transmission is assured without the distortions due to the metal gauze, while vacuum problems due to insufficient pumping of the ionization region are minimized. An image magnification factor is introduced, however, which must be determined experimentally.

In order to verify the proper functioning of the electrostatic lens as it couples with the laser source, trajectory simulations⁴ using Simion trajectory software have been carried out for a realistic experimental geometry. In the simulation, the trajectories of fragments ejected every 45° in the $x-y$ plane are traced as shown in Fig. 5(b). Trajectories starting at three points along the y axis separated by 1.5 mm are shown, beginning in Fig. 5(c) and ending in Fig. 5(d). As seen in the figure, fragments with the same velocity arrive at the same point (and also at essentially the same time) on a focal plane (where a dual-microchannel plate/phosphor screen PSD should be placed). All fragments with the same velocity focus at the same point on the PSD, irrespective of their initial starting point. For a given flight tube length and a fixed set of electrodes, the proper repeller/extractor ratio can be found from the simulations, or experimentally. The overall size of the

focused velocity pattern at the detector is then determined by the magnitude of the repeller voltage.

Trajectory simulations also confirm that the time (TOF) between photoionization and impingement on the PSD for any ion of mass m is given by $\text{TOF} = C \times [m/q]^{1/2}$, where C is a constant. The final ion velocity along x , the TOF axis, is much greater than the recoil velocity; thus the ion packet is flattened before striking the PSD. Under these conditions, \mathbf{v}_y and \mathbf{v}_z , the velocity components of the fragment ions in the transverse y and z directions are converted to positions on the PSD. Information on \mathbf{v}_x is lost, but when using light linearly polarized along z (axis defined in Fig. 3), the Newton sphere will have cylindrical symmetry around z ; thus \mathbf{v}_x contains no additional information. The PSD converts the fragment ions to flashes of light on a phosphor screen and a CCD camera records the positions of the light flashes for several thousand laser pulses, building up a data file which is stored in the laboratory computer. The original 3-D sphere is then reconstructed from the raw data file using the inverse Abel transformation. A slice through the middle of the inverted 3-D sphere is a representation of the angle-velocity spectrum of the fragments.

Conventional ion-imaging experiments with gauze-covered electrodes have a homogeneous electric field along the x direction. For an isotropic Newton sphere, most of the ions when projected on the 2-D detector, lie at the outer edge of the disk, forming thus a circle of radius

$$R = v \times \text{TOF} = [2 \times \text{KE}/m]^{1/2} \times C \times [q/m]^{1/2} = C' \times [\text{KE}]^{1/2}. \quad (1)$$

This equation holds for all charged particles, regardless of mass. In other words, with the detector time-gated at the proper TOF, any species with the same kinetic energy will appear at the same radius on the detector. This is quite helpful in calibrating signals where a molecular parameter, the bond dissociation energy, for example, is unknown. Note also that $\text{KE}^{1/2}$ is mapped instead of momentum or velocity. Velocity imaging has the same properties except that a magnification factor appears in the equation for R . This factor, and the proper repeller/extractor ratio for a set time-of-flight length, depends on the apparatus and is easily found by experiment or by trajectory simulation.

2.1.1. Resolution: Factors Affecting Image Quality

Space charge is the most important problem in the imaging experiment. Quite often the target product can only be detected by REMPI with a

focused laser. Many photodissociation processes result in product kinetic energies up to ~ 3 eV, leading to Doppler-broadening of the REMPI transitions. High intensity/broadband tunable Nd:YAG- or excimer-pumped dye laser or optical parametric amplifiers (OPO)s are well-suited to ionize these fragments. Such lasers have a pulselength of a few nanoseconds, a low duty factor (10–100 pulses/sec) and are intense enough to create far too many ions per laser shot, resulting in a space charge explosion which distorts the ion spheres. Space charge problems arise when more than a few hundred ions/shot are present in the laser focus. All ions (background, parent molecules, photofragments, etc.) contribute to space charge; thus it is important to be aware especially of ions that are not directly detected. Owing to the low duty factors of most pulsed lasers, many experiments are carried out near the space charge limit.

After space charge, the combination of the number of pixels of the CCD camera and the size of a single ion event determine the image quality. PSDs are usually two micro-channelplates (MCPs) mounted in a chevron configuration, backed by a phosphor screen. A product ion causes an electron cascade through the channelplates and onto the phosphor, which emits a pulse of diffuse light that must be focused properly onto the CCD array with a camera lens or a fiber optic taper. In this process, one product ion results in a signal on the phosphor which is usually several pixels in diameter, with the size dependent on the MCP voltage. With a typical 10^6 gain, a 40 mm active diameter PSD, a CCD array of (500×500) pixels, (one pixel covers an $80 \mu\text{m}$ square), and a single ion event when transferred to the CCD, correspond typically to about a $100 \mu\text{m}$ diameter spot. Clearly, there is no great advantage to having a pixel size very much smaller than a single ion event, especially since data transfer is slower with a larger array size.

The improved spatial resolution of velocity imaging can be quantified by an apparatus peak-width (FWHM) function, W , which describes the broadening of an initially narrow ion sphere radius. Experimentally, we find under optimal conditions W is $\sim 25 \times \text{KE}^{1/2}$ meV, thus ~ 25 meV for a particle with a 1 eV KER. The peak of this curve can, of course, be determined more accurately, e.g., within a tenth of its width. Consider a particle with 1 eV kinetic energy forming a circle with a radius of 8 mm, thus 100 pixels. At 100 pixels, the energy spacing per pixel is ~ 20 meV. With an SIE covering ~ 1.5 square pixels, the apparatus function will then

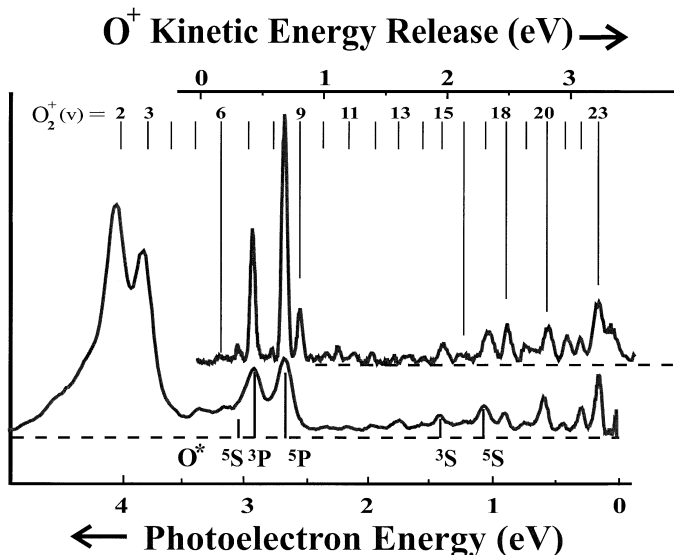


Fig. 6. Kinetic energy distributions from photofragment images of O^+ and of photoelectrons, from REMPI of O_2 at 226 nm. Two main signal channels are labeled; production (O^+) and photoionization (e^-) of $\text{O}_2^+(v)$, and production and photoionization of excited Rydberg O atoms.

be $W \sim 1.5 \times 20 \times \text{KE}^{1/2}$ meV, with KE in eV; thus $W = 52$ meV at 3 eV (173 pixels), 30 meV at 1 eV (100 pixels), and 10 meV at 0.1 eV (32 pixels). At even lower KE, the limited number of pixels will eventually restrict the resolution. These are only rough indications because the shape and size of the SIE is irregular and grows with the MCP gain.

As an example of the resolution possible with velocity mapping, the kinetic energy distributions obtained from integrating an inverted image over all angles for each value of R of an O^+ and photoelectron image produced by 2 + 1 REMPI of O_2 at 225.6 nm, are shown in Fig. 6. This is a very convenient system for testing the detector since as many as 30 well-spaced nestled Newton spheres appear in each image. The measured peak widths for the sphere radii agree well with the above values, except at the lowest kinetic energies where splitting of the peaks due to spin-orbit effects in the precursor O_2^+ results in extra broadening. Figure 6 is an example of the photophysics of superexcited states, which are discussed in more detail in the final section of this chapter.

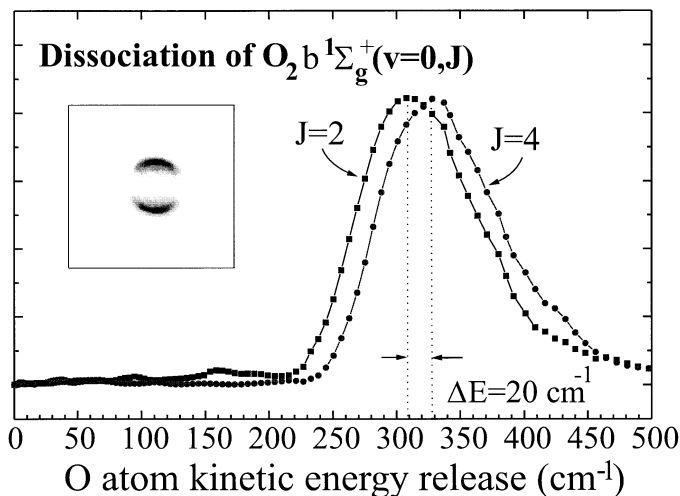


Fig. 7. Threshold photodissociation of O_2 via the $b^1\Sigma_g^+$ state.

Velocity mapping, as mentioned previously, maps distance instead of time in the TOF formula $v = \Delta d / \Delta t$. Very small velocities are just as easily measured as large velocities and this is in sharp contrast to the TOF method. Reisler and coworkers,¹⁸ in studies of near-threshold dissociation processes in HNCO, have put this feature to great advantage. Another illustration of the near-threshold capabilities of velocity mapping is given in Fig. 7, where the KE distributions for $\text{O}(^3P_2)$ atoms produced by photodissociation of O_2 , which has been selectively excited to the $b^1\Sigma_g^+(v=0, J=2$ and $J=4)$ states are shown. In this experiment,¹⁹ the highly forbidden $X^3\Sigma_g^- \rightarrow b^1\Sigma_g^+$ transition is driven with an intense-pulsed laser at 763 nm, and the REMPI detection laser at 225 nm both dissociates the $b^1\Sigma_g^+$ state and causes 2+1 REMPI of the nascent $\text{O}(^3P_2)$ atoms. Photons from the $\text{O}(^3P_2)$ REMPI laser have just enough energy to excite the molecule to the second dissociation limit, where an $\text{O}(^3P_2)$ and an $\text{O}(^1D_0)$ atom are created. On photodissociation of the $b^1\Sigma_g^+$ state, the $J=2$ level receives 308 cm^{-1} of KER while the $J=4$ level receives 328 cm^{-1} . A raw image for fragmentation of the $J=2$ level is shown as an inset in Fig. 7. From the $\sim \cos^2 \theta$ angular distribution, it can be concluded¹⁹ that the upper state in the dissociation process is the $B(^2\Sigma_u^-)$ state. As seen in Fig. 7, the $\sim 20 \text{ cm}^{-1}$ difference in rotational energy of the b state molecules is

confirmed as a $\sim 20 \text{ cm}^{-1}$ shift in the KER curve towards higher energy for $J = 4$. The overall width of the two peaks is larger than the value expected above from the apparatus function. This is because the image itself is small, thus the number of pixels limit the resolution, i.e., the energy spacing between pixels is similar to the width of the apparatus function.

To circumvent the above limitations due to the SIE size, one could consider using a single “hot” microchannel plate which should yield a much smaller spot size than a dual-plate assembly, or to use event counting, where the center of each SIE is calculated and separately stored. Such “centroiding” is common in photoionization studies using XUV photons and can give spatial resolution higher than that of the detector array. Event counting has been demonstrated for velocity mapping²⁰ and measurement software programs are commercially available. However, data acquisition devices faster than those presently available are needed for efficient use. As an estimate for the feasible resolution of velocity mapping, assume a large PSD of 120 mm active diameter and a large pixel array of $\sim 4000 \times 4000$, or 1000 pixels at the radius corresponding to 1 eV kinetic energy. If the uncertainty in the initial ion position can be decreased to 20 μm using event counting, an apparatus function of 2 meV (16 cm^{-1}) at 1 eV is predicted. At this resolution, rotational energy spacing may become resolvable. With the current rapid technical progress in PSDs and CCDs, these apparatus demands should be met in the near future. In the meantime, more detailed resolution of a portion of the image can also be achieved by magnifying the image using the electrostatic lenses or a longer time-of-flight tube to allow the image to exceed the detector size.

Other factors which affect the image quality include the initial velocity spread in the molecular beam, the internal energy spread in the parent molecule, and numerous possible experimental imperfections. The contribution of the initial velocity spread in a well-skimmed supersonic expansion is usually negligible, corresponding to an energy spread much less than 1 meV. Also important is the internal energy of the parent molecule since rotation (see Fig. 7) and vibrational modes often couple directly into the dissociation coordinate, adding a spread biased towards higher translational energies. Supersonic cooling helps to lessen this effect, but vibrational modes in the 15–100 meV range, which are thermally populated before the expansion, do not always cool efficiently. Non-crossings of ortho-para rotational manifolds during the collisional relaxation of small symmetric molecules such as H_2 , also limit the degree of rotational cooling.

Other capabilities of velocity imaging have been described in previous articles.^{20,21} An interesting demonstration is the imaging of D^+ and photoelectrons following $2+1$ REMPI of D atoms formed in an electric discharge at the nozzle of a pulsed D_2 beam. These D atoms are cooled slightly in the nozzle expansion and ionized using a focused laser operating at 243 nm. At the crossing point of the laser beam, the molecular beam is ~ 2 mm wide, which translates to ~ 20 pixels at the detector. Ion recoil from the photoionization event yields 1.7 eV photoelectrons, and ~ 0.4 meV D^+ ions. By simply reversing the polarity of the repeller/extractor fields, either D^+ or e^- can be imaged. Both show the same angular distribution, as expected from momentum conservation. The D^+ signal, however, has a radius of ~ 3 pixels while the molecular beam dimension is ~ 20 pixels. This demonstrates that velocity imaging is capable of mapping a velocity distribution smaller than the size of the molecular beam.

3. Applications of Velocity Mapping

3.1. *Decomposition of Absorption Continua: Neutral Product Analysis*

One field where velocity mapping is making an important impact is in the decomposition of overlapped absorption continua. These can be continua from direct repulsive states (Fig. 4(a)) or from the repulsive wall of bound states (Fig. 4(b)), or a combination of the two. Halogen-containing species are a good example of the former while molecular oxygen is an example of the latter category of direct photodissociation. The information provided from these efforts has both fundamental and practical applications. From the data on decomposition of the lowest energy so-called *A*-band continuum of the halogen-containing molecules, the most basic ideas on absorption strength, spin-orbit coupling, and non-adiabatic curve crossing can be tested. Symmetry-forbidden transitions dominate the lowest so-called Herzberg continuum of molecular oxygen, and data on the different components of this continuum provide a good test for the understanding of intensity-borrowing mechanisms in molecular spectroscopy. There are obvious practical applications in atmospheric photochemistry for these species, and in the characterization of hot atom sources for chemical dynamics studies. As mentioned in the introduction, the spectra of all small molecules contain regions of continuous absorption especially towards the